

LOW ENERGY-HIGH FLUX NITRIDATION OF METAL ALLOYS: MECHANISMS, MICROSTRUCTURES AND HIGH TEMPERATURE OXIDATION BEHAVIOUR

NITRIRANJE KOVINSKIH ZLITIN S FLUKSOM Z MAJHNO ENERGIJO IN VELIKO GOSTOTO: MEHANIZMI, MIKROSTRUKTURE IN VISOKOTEMPERATURNO OKSIDACIJSKO VEDENJE

Fernando Pedraza

Université de La Rochelle. Laboratoire d'Etudes des Matériaux en Milieux Agressifs (LEMMA, EA 3167). Avenue Michel Crépeau, 17042 La Rochelle cedex 01, FRANCE
fpedraza@univ-lr.fr

Prejem rokopisa – received: 2007-09-17; sprejem za objavo – accepted for publication: 2008-06-07

Nitridation is typically carried out to improve wear and erosion of different metal and alloy substrates. In the case of "stainless" alloys, the nitridation temperature needs to be lowered to avoid the precipitation of CrN that would reduce the overall corrosion resistance. Low energy – high flux nitridation allows to nitride relatively thick layers in short times at low temperatures depending on the substrate crystal structure and chemical composition as shown for pure Ni, a Ni-20Cr model alloy, a conventional AISI 304L stainless steel and an ODS FeAl intermetallic alloy. The mechanisms of nitridation, the phases and microstructures are discussed in this work with the support of X-ray diffraction, atomic force, scanning and transmission electron microscopy techniques.

The high temperature oxidation behaviour of the nitrided matrices is thereafter evaluated in air and the results are compared to non nitrided specimens. The oxidation kinetics are determined with thermogravimetry and the mechanisms are discussed in light of the oxide phases and microstructures resulting from the previous nitridation treatment. It will be shown that a reduction of the high temperature oxidation resistance occurs for the shortest oxidation times because of trapping of the protective elements.

Key words: nitridation, ion implantation, nitrided layer, austenite alloys, ODS Fe-Al alloys, surface oxidation

Nitriranje poveča obrabno in erozijsko odpornost podlag iz kovin in zlitin. Pri nerjavnih jeklih je treba znižati temperaturo nitriranja, da bi se izognili izločanju CrN, ki bi zmanjšalo splošno korozijsko odpornost. Nitriranje s fluksom z majhno energijo in veliko gostoto omogoča, da se ustvarijo relativno debeli sloji v kratkem času in pri nizki temperaturi, odvisno od mikrostrukture in kemijske sestave podlage, kot je prikazano za čisti Ni, modelno zlitino Ni-Cr20, konvencionalno jeklo AISI 304 L in za intermetalno zlitino FeAl ODS. V tem delu razpravljamo o mehanizmu nitriranja, fazah in mikrostrukturah na temelju rezultatov difrakcije rentgenskega sevanja, opazovanja atomske sile ter vrstične in presečne elektronske mikroskopije. Ocenili smo visokotemperaturno vedenje nitriranih matic na zraku in ga primerjali z nenitriranimi vzorci. Kinetiko oksidacije smo ugotovili s termogravimetrijo in o rezultatih razpravljamo z upoštevanjem oksidnih faz in mikrostruktur, ki so nastale pri nitriranju. Ugotovili smo, da se zmanjša visokotemperaturna oksidacijska odpornost pri najkrajših časih oksidacije zaradi ujetja varovalnih elementov v pasti.

Gljučne besede: nitriranje, ionska implantacija, nitrirana plast, avstenitne zlitine, Fe-Al ODS zlitina, oksidacija površine

1 INTRODUCTION

Nitriding of austenitic stainless steels has been extensively studied owing to the significant improvements in surface hardness and tribological behaviour¹ as well as in corrosion resistance² so long as precipitation of CrN is avoided³. All these improvements obtained at moderate temperature ($T < 450$ °C) seem to be associated with the formation of an interstitial solid solution of nitrogen in the steel matrix: face centred cubic (fcc) γ_N or "expanded austenite". Various studies suggest that the γ_N would correspond to a fcc phase with a high density of stacking faults likely induced by the internal stresses in the nitrided layer⁴⁻⁶.

However, the effect of the nitriding process to other alloy systems has been poorly investigated to date. For high temperature applications, Ni-base superalloys are typically employed as they show good corrosion and

oxidation resistance and excellent resistance to creep and rupture at high temperatures⁷. However, they exhibit poor wear resistance. Therefore, plasma nitriding studies have been carried out for instance on Inconel 718 (containing the mass fraction of Cr 20 %) at temperatures between 550 °C and 750 °C leading to precipitation of chromium nitride, CrN, and subsequent increase in Knoop hardness⁸ and wear resistance until the nitrided layer is worn away⁹. Further studies on plasma assisted nitriding of Inconel 690 (containing the mass fraction of Cr 30 %) have been carried out at temperatures between 300 °C and 400 °C¹⁰ where the different depths of nitrogen diffusion have been related to the grain orientations and the anisotropic dependence of stress on strain¹¹.

The low energy-high flux nitrogen implantation approach has rarely been addressed. This is also known

as an implantation-diffusion technique at relatively low temperatures to promote nitrogen diffusion while arresting CrN precipitation in stainless steels^{5,6,12,13}. Williamson et al.¹⁴ studied a collection of 16 fcc metals nitrided under the same conditions (0.7 keV, 2 mA cm⁻², 400 °C and 15 min). It was shown that the Ni-rich alloys contained much less nitrogen with correspondingly thinner layers than the Fe-rich alloys. Besides, no nitrogen could be detected in the pure Ni specimens but an isolated diffracted peak corresponding to the Ni₃N phase. The second study dealt with the tribological properties of Inconel 600 (containing the mass fraction of Cr 16 %) in comparison with the AISI 316 stainless steel, both nitrided at 400 °C for 1 h under 1.2 keV and 1 mAcm⁻²¹⁵. Again, a thin layer with a maximum concentration of the mole fraction of N 9 % was found in the Ni-rich substrates compared to a 25 at% in the stainless steel, but still offering an increase in hardness and a reduction in wear rate.

Despite the extensive use of Ni base superalloys, their significant weight is a limitation in the aeronautic domain as fuel consumption must be reduced. To this end, various intermetallic alloys based on TiAl and on FeAl represent solid alternatives to replace the heavier Ni superalloys¹⁶. In these materials, the nitridation of TiAl have received most of the attention concerning the treatment itself¹⁷⁻¹⁹, their corrosion properties²⁰ or their high temperature behaviour²¹⁻²⁴. However, little is known on the nitridation of FeAl intermetallic alloys. To the best of our knowledge, only the oxidation kinetics and the likely mechanisms of a nitrided ODS FeAl alloy were reported by Dang et al.²⁵.

Contrary to most of the studies devoted to wear and erosion, the purpose of this work is to review the mechanisms of nitridation by implantation-diffusion (also called low energy-high flux nitridation) in different model (pure Ni, Ni20Cr), commercial (AISI 304L) and candidate materials (ODS FeAl) and the effect on their high temperature oxidation behaviour. The roles of "physics" (crystal structure, grain orientation) and "chemistry" (alloying elements) will be discussed to elucidate the mechanisms involved upon nitridation. On the basis of the resulting phases and microstructures, the high temperature oxidation behaviour will thereafter be interpreted.

2 EXPERIMENTAL

Table 1 gathers the base composition and crystal structure of the materials of study. The samples consisted of round coupons of varying diameter and 1 mm thick cut from the bars. The main surfaces were mechanically polished to a final roughness of 0.01 µm. They were then ultrasonically degreased in acetone and rinsed in 96 % ethanol.

Low energy – high flux nitrogen (N₂⁺, N⁺) implantation was carried out at LMP (Poitiers, France) with a

Table 1: Substrates major composition (wt%) and the initial crystal structure

Tabela 1: Osnovni sestavni elementi v odstotkih in začetna kristalna struktura podlag ODS-zlitine, utrjene z disperzijo oksidov

substrate	Fe	Cr	Ni	Al	Y ₂ O ₃	matrix
Ni	-	-	≈ 100	-	-	fcc
Ni20Cr	-	20	80	-	-	fcc
AISI 304L	70	20	10	-	-	fcc
ODS* FeAl	60	-	-	38	2	ordered B2

* ODS = oxide dispersion strengthened

Kaufman type ion source at 1.2 keV and a current density of about 1 mAcm⁻² for 1 h, corresponding to an estimated dose of about 2.25 · 10¹⁹ cm⁻². The temperature of the samples was carefully controlled with a thermocouple attached on the back of the samples. Prior to the nitridation treatment, Ar⁺ sputtering (1.2 keV, 0.5 mAcm⁻² for 15 min) was carried out on each main coupon face to remove the rigid oxide layer that precludes nitridation²⁶. The backing pressure in the chamber upon the nitriding process was better than 10⁻² Pa. Implantation was carried out on both principal coupon faces for the subsequent oxidation experiments, representing about 85 % of the overall surface. Oxidation of the nitrided specimens was conducted in a Setaram TG92 thermobalance of 10⁻⁶ g of accuracy at 800 °C for 24 h under synthetic air. Heating and cooling rates were fixed at 50 °C/min.

Thermodynamic calculations have been performed using the HSC Chemistry software²⁷ to assess the thermodynamically stable compounds expected to form within the different matrices. The calculations have been carried out at equilibrium conditions at 10⁻² Pa (implantation conditions) and at atmospheric pressure (after implantation) disregarding collision cascades and sputtering of the surfaces. Only the gas species N₂⁺ (g) or N₂ (g) have been considered to react with the substrates, thus taking into account the splitting of the molecules into 2 nitrogen atoms and the corresponding energy release.

The characterisation of the implanted and the oxidised specimens was undertaken using contact mode atomic force microscopy (AFM) with an Autoprobe CPR (Veeco Instruments), by X-ray diffraction in a Bruker AXS D-5005 equipment in the θ -2 θ configuration and grazing incidence (GIXRD) using Cu K α_1 (λ = 0.15406 nm) radiation as well as by scanning electron microscopy (SEM) coupled to energy-dispersive spectrometry (EDS) in a JEOL JSM-4510 LV. Cross sections of the implanted specimens were also prepared for transmission electron microscopy (TEM) studies in a JEOL-JEM 2010 operating at 200 kV. For such purpose, careful mechanical polishing in SiC# 4000 emery paper was performed down to a thickness of about 50 µm. Then, Ar bombardment at 3 keV was carried out in a GATAN PIPS™ (precision ion polishing system) model 691 at

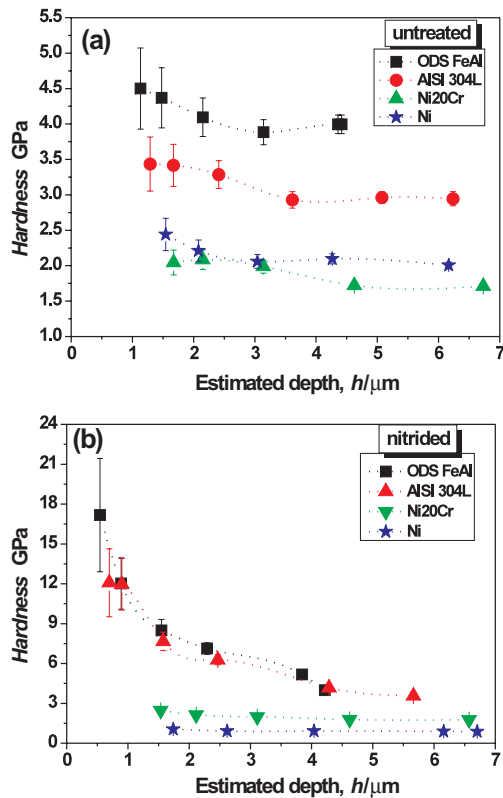


Figure 1: Evolution of Vickers microhardness with estimated depth of the (a) untreated specimens and (b) nitrided by implantation-diffusion –NID-

Slika 1: Evolucija mikrotvrdoe po Vickersu z ocenjeno globino; (a) nenitriran vzorec (b) nitriran z ionsko implantacijo in difuzijo – NID

different angles. Vickers microhardness measurements were also performed at increasing loads to get acquainted of the effects of the implantation.

3 RESULTS AND DISCUSSION

3.1 Nitridation by implantation-diffusion

After nitridation, all the substrates undergo increased surface microhardness compared to the untreated specimens as depicted in **Figure 1**. In comparison with the untreated specimens, the hardness increase is of about (8, 20, 250 and 280) % for pure Ni, Ni20Cr, AISI 304L and ODS FeAl, respectively. From these results, it can be considered that nitridation does not effectively occur in pure Ni. This can be due to two interconnected mechanisms. The first one is due to the incorporation of N as an interstitial solid solution and/or to the formation of hard metal nitrides, i. e. "structural deformation", i. e. the appearance of harder crystalline phases. The second one is related to an increased plastic deformation typically occurring upon implantation, i. e. "microstructural deformation", i. e. surface roughness.

Regarding the crystallographic phases, the XRD patterns after implantation clearly reveal various features and striking differences among the different substrates as shown in **Figure 2**. In the case of pure Ni [**Figure 2(a)**] the patterns of the untreated and the nitrided specimens are rather similar. Calculations of the lattice parameters of both untreated and nitrided substrates leads to the

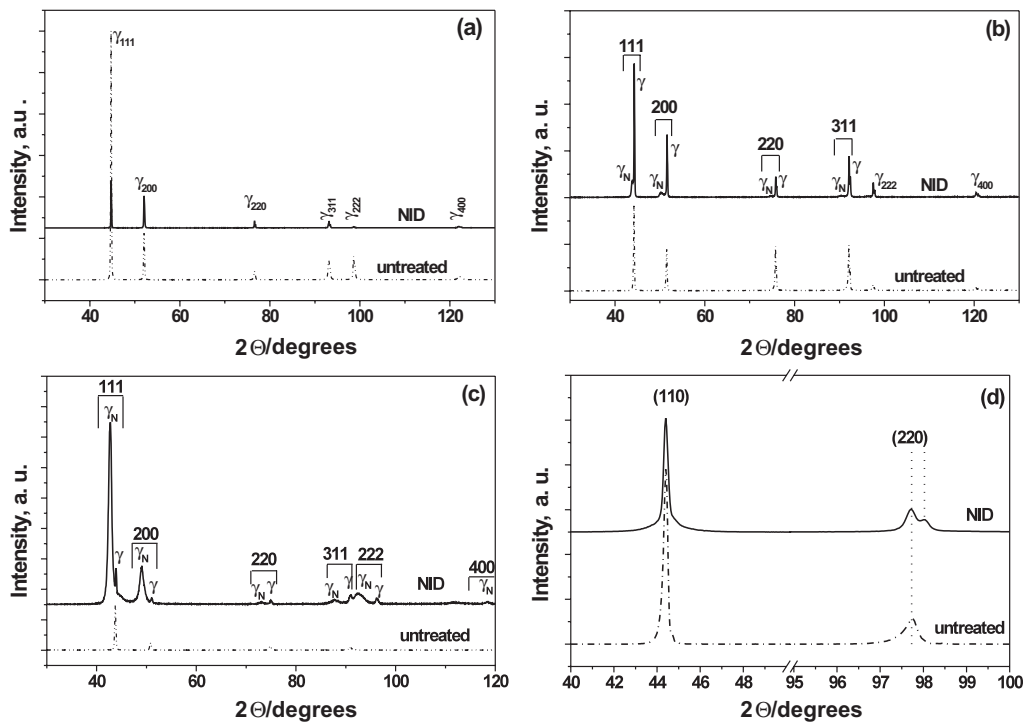


Figure 2: X-ray diffraction patterns of the different substrates untreated and nitrided by implantation diffusion –NID- (a) pure Ni, (b) Ni20Cr, (c) AISI 304L and (d) ODS FeAl

Slika 2: Diagrami difrakcije rentgenskega sevanja za različne podlage, nenitrirane in nitrirane z implantacijsko difuzijo (NID): (a) čisti Ni, (b) NiCr20, (c) AISI 304 in (d) ODS FeAl

same results ($a_0 \approx 0.351$ nm) hence indicating no expansion of the matrix volume. The only remarkable changes involves an attenuation of the $\langle 111 \rangle$ directions after nitridation compared to the untreated Ni. Williamson et al.¹⁴ also claimed the absence of γ_N peaks in pure Ni at a lower energy and a higher flux than in our studies. However, they observed a hexagonal Ni_3N phase and detected a small shift to lower angles, thus implying retention of a very small amount of nitrogen.

Contrary to pure Ni, the nitrided Ni20Cr and AISI 304L substrates [Figure 2(b)] exhibit a fcc γ_N phase²⁸ at lower diffraction angles and the original γ phase peaks have shifted towards higher diffraction angles²⁹. For the sake of comparison between both implanted Cr-containing substrates a rough estimation of the retained nitrogen has been carried out using the Vegard's law for substitutional solid solution as follows: $a_{\gamma N} = a_{\gamma} + \alpha \cdot C_N$, where $a_{\gamma N}$ and a_{γ} are the lattice parameters for the N-containing and N-free γ phases, respectively, and α is the Vegard's law constant (0.00072 for Fe alloys, also assumed for Ni alloys in this study¹⁴). The concentration of nitrogen is the mole fraction in $x(N)\%$. The results are gathered in Table 2.

Table 2: Lattice parameters of the N-containing γ_N and N-free γ austenite phases, the relative expansion induced, and their corresponding average atomic nitrogen contents, $x(N)\%$, as a function of the diffraction plane (hkl) in Ni20Cr and AISI 304 L

Tabela 2: Mrežni parametri avstenitnih faz γ -faz z dušikom in brez njega, relativna inducirana razširitev in ustrezna povprečna atomska vsebnost dušika $x(N)\%$ za različne difrakcijske ravnine (hkl) v Ni20Cr in AISI 304L

	hkl	111	200	220	311
Ni20Cr	$a_{\gamma N}/nm$	0.3580	0.3637	0.3589	0.3612
	a_{γ}/nm	0.3538	0.3540	0.3545	0.3548
	expansion/%	1.2	2.8	1.2	1.8
	$x(N)\%$	≈ 6	13.5	6	≈ 9
AISI 304L	$a_{\gamma N}/nm$	0.3666	0.3716	0.3666	0.3683
	a_{γ}/nm	0.3572	0.3583	0.3583	0.3583
	expansion/%	2.6	3.7	2.3	2.7
	$x(N)\%$	13	18.5	11.5	14

Table 2 shows that the retained amount of nitrogen is highly anisotropic. In Ni20Cr the N content is significantly lower than in the AISI 304L steel regardless of the crystallographic plane. In both substrates however, the highest amount of nitrogen seems to concentrate in the (200) planes and the lowest in the (220). The different partitioning of nitrogen in the various planes also brings about different expansion of the lattice, which in turn may induce strains and stresses. Menthe et al.³⁰ suggested that a tetragonal distortion of the fcc phase had occurred whereas Fewell et al.³¹ proposed a triclinic distortion. Marchev et al.^{32,33} considered instead the formation of a martensitic phase. However, any of these would imply the presence of extra peaks never observed on the diffraction patterns. A new structural

model nitrogen expanded austenite has been recently proposed by Blawert et al.⁴ assuming the effects of deformations and twin faulting commonly observed in fcc metals or alloys. The γ_N expanded austenite would correspond to a fcc phase with a high density of stacking faults likely induced by the internal stresses existing in the nitrided layer^{5,6}. Indeed, it has been shown that the presence of stacking and twin faults in a perfect fcc lattice produces angular displacements of peaks in XRD patterns³⁴. The three nitrogen solid solutions observed by Leroy et al.¹⁰ after plasma nitriding of the Ni base alloy Inconel 690 (Ni-30Cr-10Fe, w/%) has not been observed in this work using low energy-high flux implantation.

In the ODS FeAl intermetallic, the major contribution arises from the (110) and (220) reflections before and after nitridation. At grazing incidence, the hexagonal AlN appears as inferred by three XRD peaks ($2\theta = 33.2^\circ, 36.1^\circ$ and 38°) and a large and high (110) peak corresponding to the substrate matrix²⁵. In this alloy, the chemical affinity of N to Al is much greater than that to Fe (e. g., $\Delta H_f^\circ = -318.0$ and -10.5 kJ mol⁻¹ for AlN and Fe₄N, respectively)³⁵ and thus iron nitride formation was not expected to occur.

The surface state after nitridation is also quite different among the substrates as shown by plane view SEM in Figure 3. In pure Ni some grains are darker and the orientation of the dislocation slipping bands composing each grain is underpinned; while other grains are lighter in colour and of smoother appearance. In addition, a significant number of protrusions appear throughout the entire surface, especially at grain boundaries. AFM investigations confirm that the roughness can vary between 17.5 nm and 27.5 nm and the aligned bands can be ascribed to the slipping bands due to the presence of stress, as also reported in fcc AISI 316 L stainless steel³⁶. In Ni20Cr the surface is rather uniform and smooth with no protrusions but with relatively coarse pores. The average roughness is of about 5 – 8 nm but more significant height differences among grains compared to nitrided Ni. The AISI 304L surface is the most heterogeneous of all three fcc nitrided substrates. Some grains are very smooth and deeper and contain large pores thus reminding of the Ni20Cr grains, whereas other grains resemble more the nitrided Ni by underlining the slipping bands, hence being rougher. A common feature observed on the three fcc alloys is the occurrence of twinning within the grains, but again the morphology of twins differs from one matrix to the other. On the contrary, the ordered B2 cubic structure ODS FeAl, the surface seems very uniformly implanted with no twins but some protrusions at the external surface and remaining porosity. This latter feature can be mainly explained by the manufacturing process of this material, which is powder metallurgy. The elongated shape of the protrusions would be related to "softer" areas of the base material, where the strengthening effect

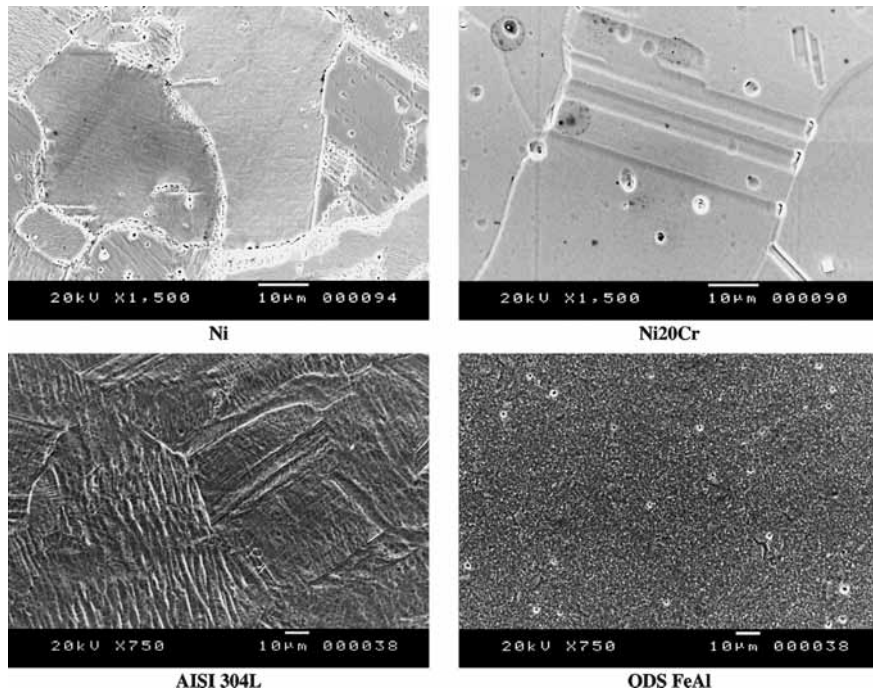


Figure 3: SEM surface morphology after low energy-high flux nitridation of (a) pure Ni, (b) Ni20Cr, (c) AISI 304L and (d) ODS FeAl
Slika 3: SEM-morfologija površine po nitriranju s fluksom z majhno energijo in veliko gostoto pri (a) čistem niklju, (b) NiCr20, (c) AISI 304 L in (d) ODS FeAl

of Y_2O_3 particles is less important, as revealed by AFM studies [Figure 4(a)]. This microstructure is accompanied by the highest roughness values, which can attain up to 50 nm.

According to the work of Pranevicius et al.³⁷, the surface roughness can derive from the competition between surface kinetics and bulk diffusion. Nucleation of roughness would first occur by relocation of adatoms, formation of surface vacancies and removal of atoms, which in turn lead to the appearance of clusters of atoms in other regions of the surface. The development of surface roughness subsequently occurs by further relocation and sputtering of atoms displaced by the ion beam. Thereafter, diffusion of nitrogen seems to occur mainly along grain and sub-grain boundaries creating compressive stresses³⁸. Within the metallic substrate, atomic nitrogen can then recombine as molecular nitrogen, raising locally the pressure and inducing plastic deformation. Therefore, the amount of deformation would depend on the yield stress of the host material. As a result, a blistered surface appears^{39,40}. Due to the recession of the metal surface upon implantation, the blisters are peeled off and the pores are then clearly visible in pure Ni and in Ni20Cr [Figure 4(b)]. Since the solubility of nitrogen in nickel is very low the observed porosity is rather shallow. The larger number of pores and blisters are however found at the grain and twin boundaries rather than within the grains as also inferred in a previous study⁴¹. This seems to support the idea that diffusion of nitrogen might be more prone to occur along these short circuit paths, which also become readily

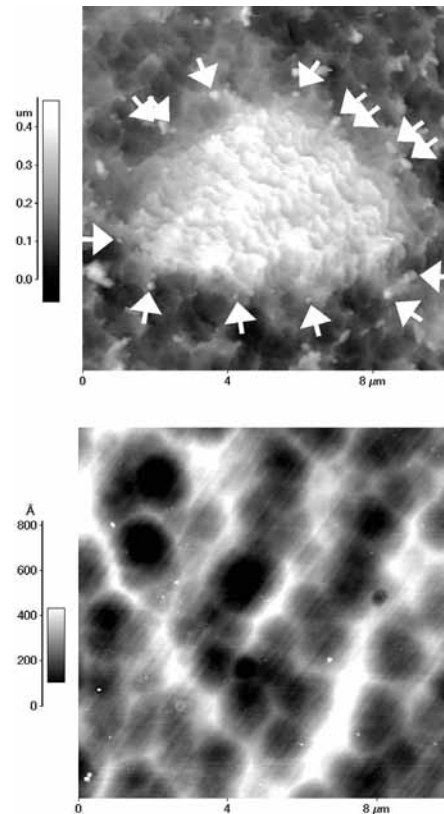
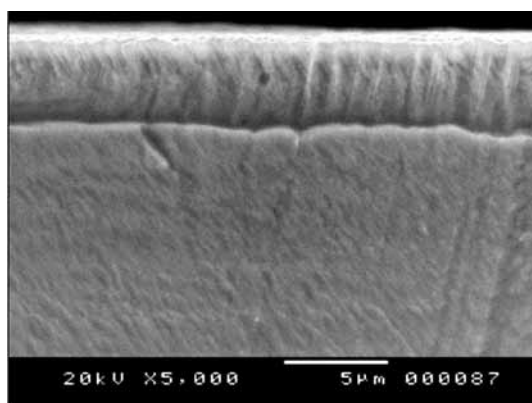


Figure 4: AFM images of (a) nitrided ODS FeAl showing ridges pinned by Y_2O_3 particles (b) nitrided Ni20Cr showing the resulting porosity (views of $(10 \times 10) \mu\text{m}$ areas)

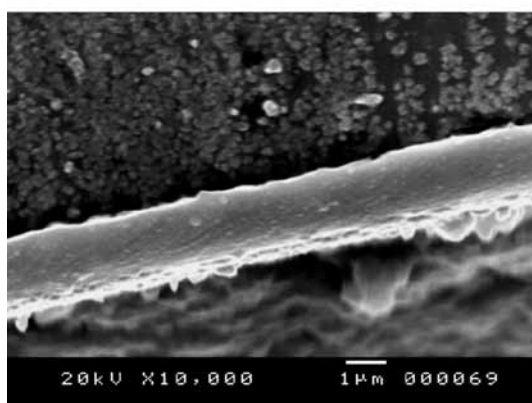
Slika 4: AFM-sliki (a) nitrirani ODS FeAl, ki prikazuje grebene, zasidrane z delci Y_2O_3 in (b) nitriranega NiCr 20, ki prikazuje nastalo poroznost (ploskvi $(10 \times 10) \mu\text{m}$)

saturated in nitrogen inducing significant plastic deformation.

Indeed, EDS microanalyses indicate that no nitrogen has been retained in pure Ni either within the grains or at the grain boundaries where more protrusions are observed. Conversely, in the Cr-bearing alloys the distribution of nitrogen is uneven and confirms the XRD results. For instance, whereas about the mole fraction of N 10 % is present at the surface of Ni20Cr regardless of the location, in AISI 304L stainless steel some of the grains only incorporate about 12 % N and some others contain up to 17 % N, which is close to the chromium content in the substrate. Because of the anisotropic incorporation of N, different compressive stresses are generated. This leads to distortions, plastic deformation and even lattice rotations in an anisotropic fashion⁴². As a result of the anisotropic deformation, heterogeneous diffusion will occur modifying the nitrogen ingress rate³⁶. On the contrary, in the FeAl intermetallic alloy the average composition is Fe-25Al-20N (X/%). This suggests that the N content being introduced could be limited by the Al amount at the surface of the substrate and therefore is only dependent on Al diffusion⁴³.



AISI 304L



ODS FeAl

Figure 5: SEM cross section of the nitrided (a) AISI 304L stainless steel and (b) ODS FeAl showing protrusions and the nanograin structure of the substrate

Slika 5: SEM-prerez nitriranega (a) nerjavnega jekla AISI 304 in (b) ODS FeAl s protuzijami in nanoznata struktura podlage

The SEM cross section morphologies clearly reveal that the only well defined nitrided layers appear on the AISI 304L and the ODS FeAl substrates after a chemical etch (**Figure 5**). However, the EDS composition profiles (**Figure 6**) indicate that N has effectively been incorporated in the Ni20Cr matrix. The maximum N content is found for the ODS FeAl alloy but the depth is the lowest because of N inward diffusion is arrested by the formation of AlN. On the contrary, the shape of the N content is similar in Ni20Cr and AISI 304L. As higher N contents are present in the steel, the nitrided layer is about 1 µm thicker in the steel than in the Ni20Cr alloy. At the substrate/nitrided layer interface, a steep N drop occurs in the steel in comparison with the Ni20Cr alloy. Some explanations can be found from thermodynamic calculations and TEM analyses. Nitrogen has a very low solubility⁴⁴ and permeability⁴⁵. Upon nitrogen implantation chromium shows a strong tendency to form either the fcc CrN ($\Delta H^\circ = -40 \text{ kJ mol}^{-1}$) or the hcp Cr₂N ($\Delta H^\circ = -38 \text{ kJ mol}^{-1}$) phases, which have not been observed experimentally in Ni20Cr. However, the hexagonal Cr₂N phase seems to precipitate at the nitrided layer / AISI 304L interface as shown by cross section TEM and selected area diffraction patterns (SADPs) (**Figure 7**, **Table 3**). Fe₂N nitride could be also present at the nitrided layer/steel interface but its heat of formation (-18 kJ mol^{-1}) suggests that Cr₂N should be the major nitride. This means that the formation of metal nitrides at the nitrided layer/substrate interface would arrest further N inward diffusion and could explain the steep drop of the N content shown in **Figure 6**.

This may indicate that Cr allows to significantly increase the N solubility in Ni. Because nickel rejects nitrogen, the nickel-rich substrate (Ni20Cr) incorporates less nitrogen. On the other hand, from a thermodynamic point of view the free enthalpy (ΔG) is more negative

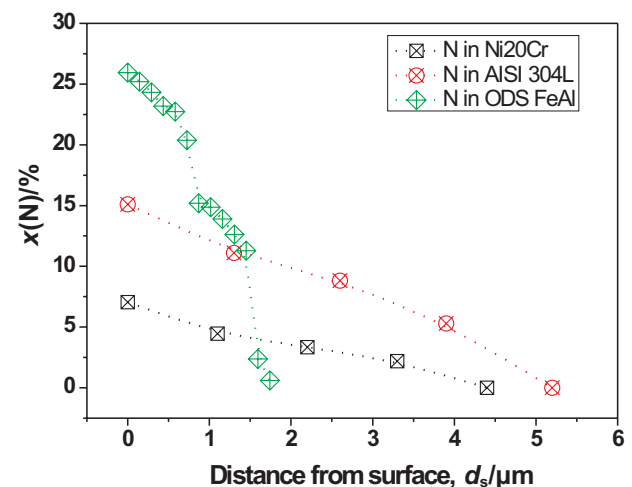


Figure 6: N profile from EDS microanalyses of the cross sections of the nitrided materials. (NB: EDS of ODS FeAl from TEM cross sections)

Slika 6: N-profil iz EDS-mikroanalize na prerezu nitriranih materialov (Opomba: EDS ODS FeAl iz TEM prereza)

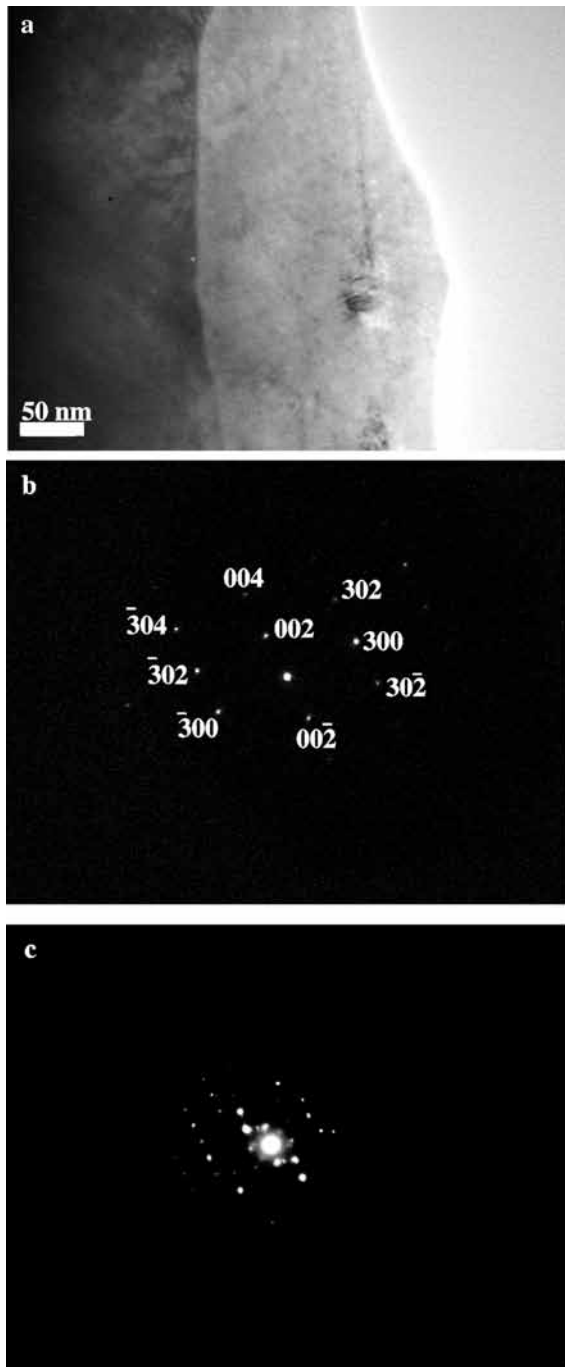


Figure 7: (a) TEM cross section of the nitrated AISI 304L stainless steel. SADPs of the (b) innermost zone corresponding to a single grain oriented [010]_{Cr2N}; and (c) outermost zone representative of various grains

Slika 7: (a) TEM-prerez nitriranega nerjavnega jekla AISI 304 L. SDAP (b) notranje cone, ki ustreza enemu zrnu z orientacijo [010]_{Cr2N}, in (c) zunanja cona, ki ima različna zrna

(thus, more spontaneous reaction) upon the formation of chromium nitrides than that of iron nitrides (**Figure 8**). However, the iron effect cannot be neglected if the chemical potential of the species is also taken into account; i. e. when one mole of nitrogen encounters the substrate surface 70 % of the atoms are composed of iron

Table 3: Data from the selected area diffraction patterns (SADPs) shown in **Figures 7 (b) and (c)** and the corresponding compounds identified by TEM

Tabela 3: Podatkih iz difrakcijskih slik izbranih ploskev (SADPs), ki jih prikazuje **slika 7 (b) in (c)**, in ustrezna spojina, identificirana s TEM

experimental <i>d</i> -spacing	γ_N (experimental)		Cr ₂ N (JCPDS 79-2159)		Fe ₂ N (JCPDS 73-2102)	
	<i>d</i> -spacing	hkl	<i>d</i> -spacing	hkl	<i>d</i> -spacing	hkl
2.40 ^c			2.37	(110)	2.39	(110)
2.25 ^b			2.21	(002)	2.21	(002)
2.10 ^c	2.10	(111)	2.09	($\bar{1}\bar{1}1$)	2.10	($\bar{1}\bar{1}1$)
1.86 ^c	1.86	(200)	1.86	(201)	1.87	(201)
1.52 ^c			1.55	(210)	1.48	(211)
1.46 ^c			1.46	($2\bar{1}1$)	1.47	(003)
1.35 ^b			1.37	(300)	1.38	(300)
1.16 ^b			1.16	(302)	1.17	(302)
0.92 ^c	not assigned		not assigned		not assigned	
0.89 ^c	0.89	(400)				

^b data from Figure 7 (b) and ^c from Figure 7 (c)

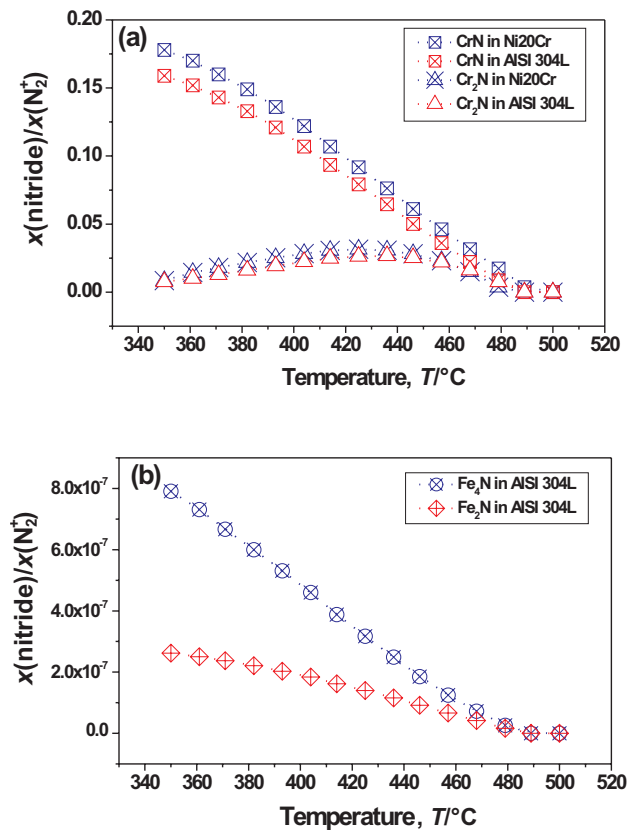


Figure 8: Evolution of mole of metal nitride produced per mole of N₂(g) as a function of temperature at 10⁻² Pa according to the HSC thermochemical calculations ²⁷ (a) chromium nitrides formation in Ni20Cr and AISI 304L and (b) iron nitrides in AISI 304L

Slika 8: Evolucija molarnosti kovinskega nitrída na mol N₂ (g) v odvisnosti od temperature pri 10⁻² Pa na podlagi termokemičnih izračunov ²⁷ (a) nastanka kromovih nitrídov v NiCr20 in AISI 304 L in (b) nitrídi železa v AISI 304 L

and only 20 % of chromium. As a result, iron can also enhance incorporation of nitrogen at least to some extent. Indeed, Rivière et al.⁵ found that nitrogen was always detected in a nitride type state and that it was preferentially bound to chromium, without specific nitride formation, which agrees well with the trapping-detrapping mechanism proposed by Möller et al.⁴⁶. Similarly, a small amount of iron atoms showed the same nitride type bonding but only at the outermost surface. Therefore, iron interaction together with a lower nickel content (which rejects nitrogen) results in higher nitrogen supersaturation in the superficial layers of AISI 304L than in Ni20Cr. Thereafter, because of the difference in chemical potentials between the external layer and the bulk, diffusion will be enhanced. As a result, the Fe-based alloy, which incorporates more nitrogen, will exhibit a higher degree of deformation. This induces significant swelling of the grains, thus developing rougher surfaces than Ni20Cr.

For the ODS FeAl intermetallic alloy, the nitrated layer has a nanostructured morphology and at the nitrated layer / substrate interface an iron band segregates (Figure 9). Diffraction patterns of the different

areas point out the different features observed in these samples such as the nanometre scale of the nitrated layer characterised by the typical rings corresponding to FeAl as well as some spots at shorter distances belonging to AlN. As summarised in Table 4, some of the distances may also correspond to α -Fe.

Sanghera and Sullivan³⁵ found that nitrogen implanted at low energy and low flux into pure aluminium did not render stoichiometric AlN because the radiation damage induced many vacancies, interstitials and defects. From our EDS analyses, only the outermost layers would contain enough nitrogen to produce the hexagonal AlN phases massively and therefore, once the average values of nitrogen decrease, a mixture of FeAl containing dispersed particles of AlN occurs closer to the nitrated layer/substrate interface. From the TEM results a combined mechanism of nitrogen diffusing inwardly and aluminium outwardly during the nitridation treatment would occur. This countercurrent diffusion would be promoted by the creation of short-circuit diffusion paths, i.e. the grain boundaries of the nanostructured layer. Indeed, diffusion of indium (isoelectronic with aluminium) has been found to be faster than that of iron by a factor of about two in Fe₆₆Al₃₄ and Fe₅₀Al₅₀⁴⁷, which helps in corroborating the suggested mechanism.

Table 4: Experimental *d*-spacings obtained with 0.15 μ m-diaphragm SADPs at the nitrated layer/substrate interface in the as-nitrated intermetallic alloy and their correspondence to the planes of the identified compounds

Tabela 4: Eksperimentalne *d*-razdalje, izmerjene pri SDPS z 0,15 μ m veliko zaslonko, na medpovršini nitridna plast/podlaga v nitrirani intermetalni spojini in njihova lega glede na ploskev indentificiranih spojin

Experimental <i>d</i> -spacing, nm	FeAl JCPDS 33-20	α -Fe JCPDS 89-4186	AlN JCPDS 25-1133
0.252	–	–	002
0.207	110	110	–
0.160	111*	–	110
0.143	200	200	–
0.119	211	211	202

* superstructure peak

3.2 High Temperature oxidation behaviour

Because of their specific uses, the oxidation tests were conducted at different temperatures and the results will be therefore presented independently.

3.2.1 Oxidation of Ni and Ni20Cr: 700 °C and 800 °C

Figure 10 shows the mass gain curves against time for both untreated and nitrated specimens. It can be observed that in nitrated Ni no significant difference is observed at both temperatures. On the contrary, in Ni20Cr nitridation increases significantly the overall mass gain. Assuming parabolic behaviour, the oxidation constants have been calculated by the $(\Delta M/S)^2$ vs. time

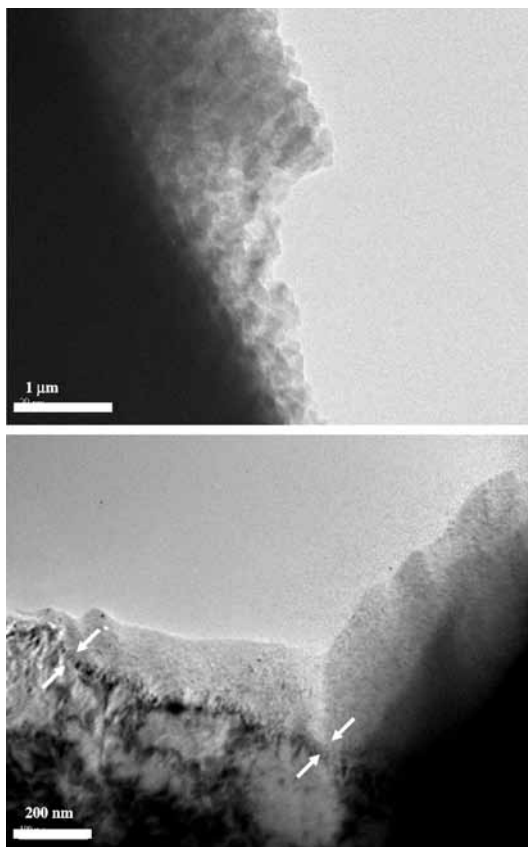


Figure 9: TEM cross section showing (a) the nanostructured morphology of the nitrated layer and (b) the nitrated layer/substrate interface. The band of α -Fe segregated at this interface is indicated between arrows

Slika 9: TEM-prerez, ki prikazuje (a) nanostrukturirano morfologijo nitridne plasti, in (b) medpovršina nitrirana plast/podlaga. Plast segregiranega α -Fe na tej medpovršini je prikazana med puščicami

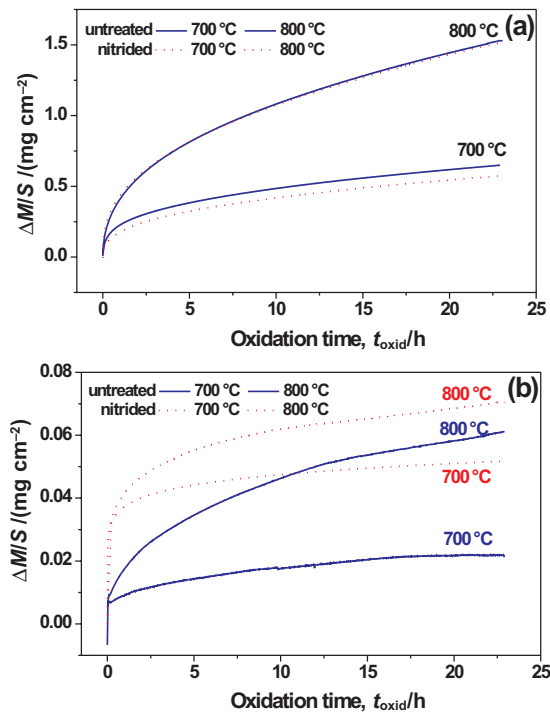


Figure 10: Isothermal oxidation at 700 °C and 800 °C for 24 h in synthetic air (a) untreated and nitrided Ni and (b) untreated and nitrided Ni20Cr

Slika 10: Izotermna 24-urna oksidacija pri 700 °C in 800 °C v sintetičnem zraku; (a) nenitriran in nitriran Ni in (b) nenitriran in nitriran NiCr20

method. In Ni, the parabolic rate constant (k_p) values of $4 \cdot 10^{-12} \text{ g}^2 \text{ cm}^{-4} \text{ s}^{-1}$ and $2.5 \cdot 10^{-11} \text{ g}^2 \text{ cm}^{-4} \text{ s}^{-1}$ are found for 700 °C and 800 °C, respectively. However, in Ni20Cr the k_p values increase about one order of magnitude from ($1.0 \cdot 10^{-15}$ to $8.3 \cdot 10^{-15}$) $\text{g}^2 \text{ cm}^{-4} \text{ s}^{-1}$ at 700 °C and from ($2.3 \cdot 10^{-14}$ to $2.3 \cdot 10^{-13}$) $\text{g}^2 \text{ cm}^{-4} \text{ s}^{-1}$ at 800 °C after the whole oxidation test.

The XRD patterns have revealed the formation of NiO oxides in both untreated and nitrided Ni samples, together with some weak peaks of the substrate, indicating a relatively thick oxide layer at both temperatures. The oxide species developed on Ni20Cr are the same for both the untreated and nitrided specimens at either temperature and these include NiO, NiCr_2O_4 and Cr_2O_3 . At the highest temperatures, more contribution of Cr_2O_3 oxide is found to occur. However, the substrate/oxide intensity ratios are always higher at any temperature than in the nickel substrates. This means that a thinner oxide layer is obtained in the Ni20Cr samples after 24 h of isothermal oxidation. Regarding the expanded austenite (γ_N) phase (Figure 11) oxidation at 700 °C for 24 h brings about shifting of the γ_N and γ peaks towards the original γ phase ($2\theta = 44.28^\circ$) giving rise to the observed doublet. This clearly implies redistribution of nitrogen in the matrix but no nitride phase can be derived from the XRD results.

The SEM morphologies are also completely different. Whereas the untreated specimens develop even and

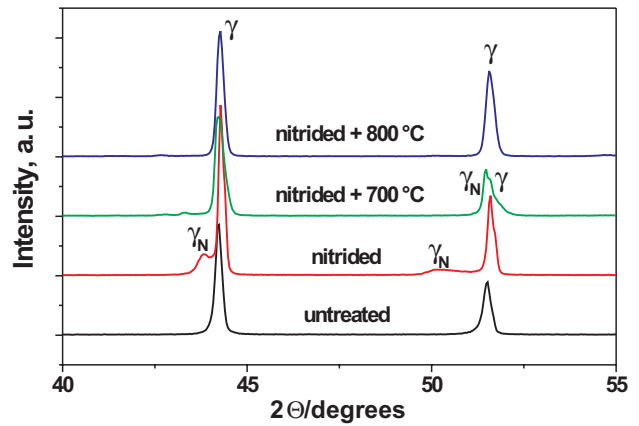


Figure 11: Selected range of the obtained on the untreated, as-nitrided and nitrided and oxidised at 700 °C and 800 °C Ni20Cr substrates. N.B: Only the matrix peaks are indicated. See text for further information concerning oxide species.

Slika 11: Izbrana področja na nenitriranem, nitriranem in nitriranem ter oksidiranem Ni20Cr podlagah. (Opomba: Prikazani so le vrhovi matrice. V tekstu je pojasnilo o vrstah oksidov).

homogeneous oxide scales, the oxide layers spall off or oxide plates develop in nitrided Ni [Figure 12(a) and (b)]. In Ni20Cr oxidation occurs preferentially depending on the grain orientation and grain boundary. At the lowest temperatures, the Ni20Cr samples are distinctively covered of oxides [Figure 12 (c) and (d)], which are more developed at 800 °C [Figure 12(e) and (f)],

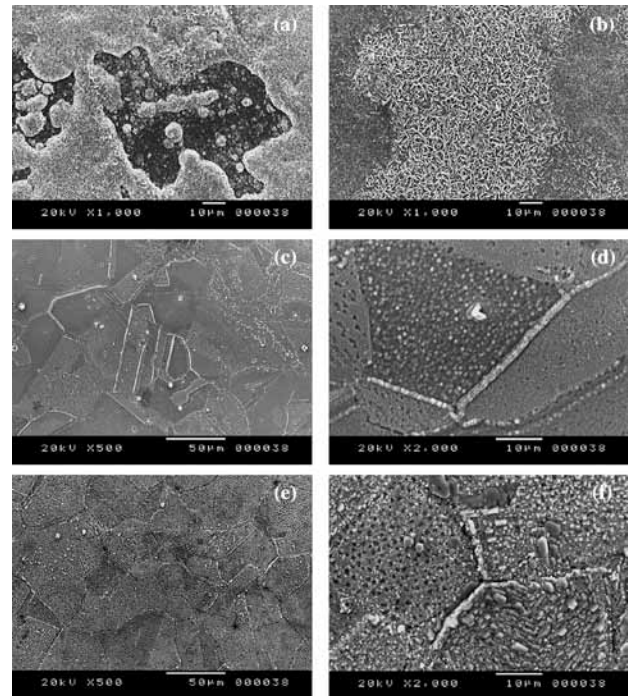


Figure 12: SEM surface morphologies developed at high temperature on (a) and (b) nitrided Ni at 700 °C and 800 °C; (c) and (d) nitrided Ni20Cr at 700 °C and (e) and (f) Ni20Cr at 800 °C

Slika 12: SEM-morfologija površin, ki so nastale pri visoki temperaturi na (a) in (b) nitriranem Ni pri 700 °C in 800 °C, (c) in (d) nitriranem Ni20Cr pri 700 °C in (e) ter (f) pri 800 °C

thus suggesting that the N implantation effect is lost at the highest temperature, as confirmed on the cross sections by SEM and EDS microanalyses. Indeed, the N content drops from about the mole fraction 10 % at the surface of the as-nitrided specimens to 3.5 % and 0 % after 24 h of oxidation at 700 °C and 800 °C. At 800 °C, some tiny metal nitrides precipitate (about 3 % N).

3.2.2 Oxidation of AISI 304L: (400, 450, 500 and 550) °C

Figure 13 shows the mass gain curves as a function of time for both the untreated **[Figure 13 (a)]** and the nitrided **[Figure 13 (b)]** specimens. Oxidation is more significant in the nitrided samples than in the untreated steel upon the first oxidation times at any temperature as a result of both a chemical and physical effect ⁴⁸. The first one is related to the amount of implanted nitrogen, whereas the second refers to the defects induced upon implantation.

The XRD patterns of the untreated steel show mainly the substrate peaks, i. e. austenite γ and ferrite α phases are observed, indicating the low thickness of the scale. The small participation of the ferrite α phase has been previously reported to occur as a result of both plastic deformation induced upon grinding ⁴⁹ and after high temperature exposure due to chromium outward diffusion, which partially destabilise the γ austenitic phase until oxide formation is accomplished ⁵⁰. Only in

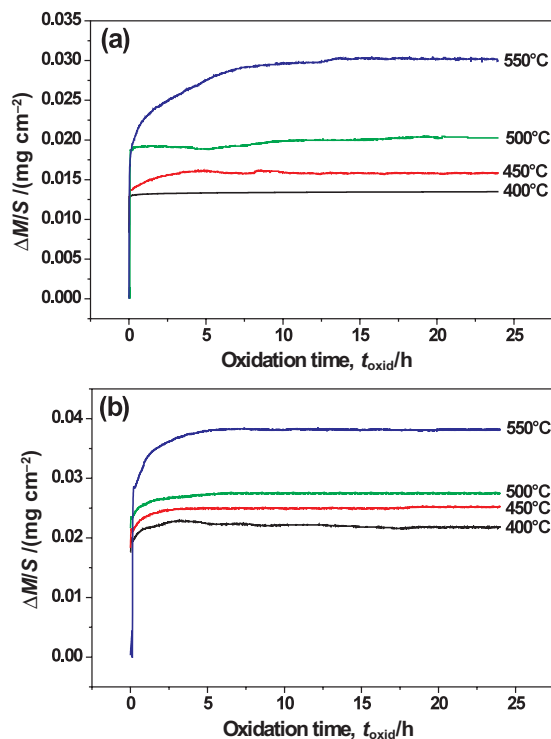


Figure 13: Isothermal oxidation of the AISI 304L stainless steel at 400, 450, 500 and 550 °C for 24 h in synthetic air (a) untreated and (b) nitrided

Slika 13: Izotermna oksidacija nerjavnega jekla AISI 304 L 24 h pri (400, 450, 500 in 550) °C v sintetičnem zraku; (a) nenitrirano, (b) nitrirano

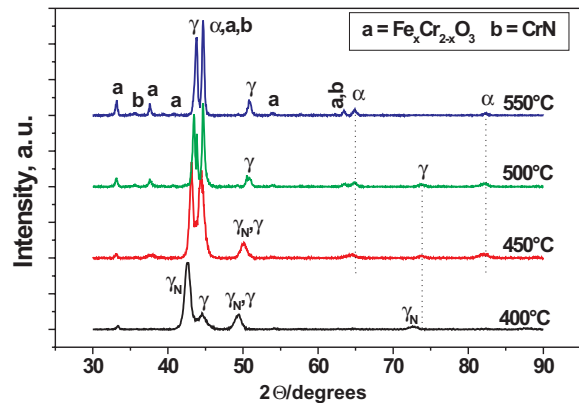


Figure 14: GIXRD patterns at 15° of the nitrided AISI 304L stainless steel after oxidation in air for 24 at 400, 450, 500 and 550 °C

Slika 14: GIXRD-odsevi pri 15° za nitrirano nerjavno jeklo AISI 304L po 24-urni oksidaciji na zraku pri (400, 450, 500 in 550) °C

GIXRD at 15° a weak hematite (α -Fe₂O₃) signal appears at 550 °C.

In the nitrided specimens, the γ_N phase is present up to 500 °C **[Figure 14]** but it evolves towards a more stable state, which implies rejection of nitrogen in solid solution in the nitrided layer. Mändl et al. ⁵¹ after annealing of a nitrided austenitic stainless steel at 425 °C found that the lattice expansion was considerably reduced, yielding a new γ_{N2} phase and additional CrN peaks under 8° of incidence. The XRD results of **Figure 14** indicate that the decomposition of the γ_N phase occurs by formation of CrN and two other FeNi phases α (bcc) and γ (fcc) probably containing a small amount of Cr. The precipitation of the cubic CrN phase is detected from 500° C since at 400°C the mobility of chromium in the AISI 304L stainless steel is low ⁵². The presence of the α phase can be explained as for the untreated steel (see above) as well as from the nitrogen partial dissolution from the (Fe,Cr)₂N leading to a α' -(N) martensite ⁵³. This fact, together with the substantial decrease of superficial nitrogen observed by EDS, indicates that upon oxidation, nitrogen may mainly diffuse inwardly towards the bulk. Such diffusion coupled to the outward diffusion of chromium from the bulk alloy gives rise to the more thermodynamically and kinetically stable CrN nitride. Öztürk and Williamson ⁵⁴ also found the formation of CrN upon the post-annealing of the AISI 304 stainless steel at 400 °C. However, decomposition of such phase was not observed even after 36 h but a dramatic reduction in N content due to inward and outward diffusion.

The oxide scales developed in the untreated steel evolve mainly through bulk alloy outward diffusion and not via the grain boundaries **[Figure 15 (a) and (b)]**. On the contrary, oxide development is more pronounced on the surface of the nitrided steel even at the lowest oxidation temperatures as a result of the deformation induced through ion implantation **[Figure 15 (c)]**. Again, as the oxidation temperature increases, the oxide cove-

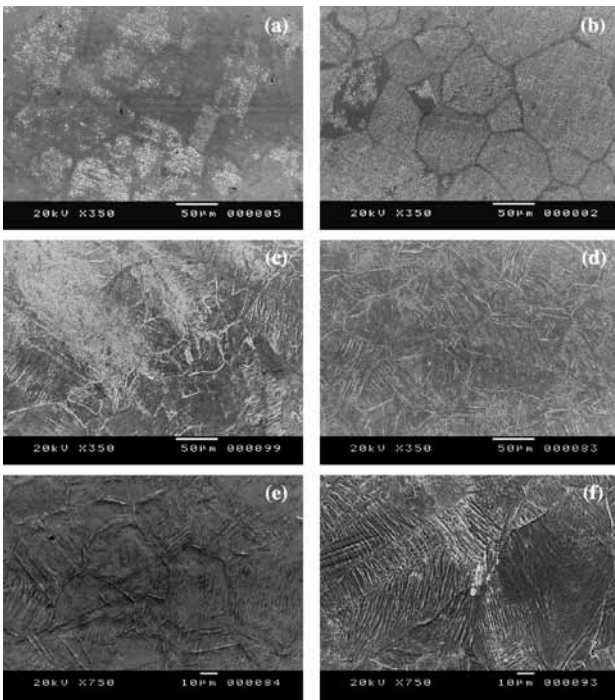


Figure 15: SEM surface morphologies developed the AISI 304L stainless steel (a) and (b) untreated and oxidised at 500 °C and 550 °C, respectively; and of nitrided and oxidised at (c) 400 °C, (d) 450 °C, (e) 500 °C and (f) 550 °C

Slika 15: Morfologija površine, nastale na nerjavnem jeklu AISI 304L: (a) izhodna in (b) oksidirana pri 500 °C in 550 °C; nitrirana in oksidirana pri (c) 400 °C, (d) 450 °C, (e) 500 °C in (f) 550 °C

rage increases depending on the roughness of each grain [Figures 15 (d), (e) and (f)]. Contrary to the untreated steel, diffusion seems to occur through both the bulk alloy and the grain boundaries.

The EDS microanalyses show the only presence of oxygen, chromium and iron on the scales (Figure 16). It can be observed that oxide formation is clearly promoted with increasing temperature whereas the superficial nitrogen content decreases. The ratios Fe/Cr after oxidation of the untreated steel at any temperature are relatively the same in comparison with the unoxidised steel. According to the cross section analyses, the oxidising temperature seems to provide enough energy to induce chromium and nitrogen diffusion so that tiny precipitation of CrN might occur as for the Ni20Cr substrates. This in turn leads to the γ_N disappearance and the formation of the α phase. Öztürk and Williamson⁵⁴ observed the vanishing of the magnetic state of the γ_N phase as the post-annealing treatment of the fcc AISI 304 steel at 400 °C progressed with time, in agreement with the above results.

3.2.3 Oxidation of ODS FeAl: 800 °C

After the 24 h exposure at 800 °C, the weight gains of the nitrided specimens was four-fold that of the un-nitrided, with k_p values of about $4.7 \cdot 10^{-8} \text{ mg}^2 \text{ cm}^{-4} \text{ s}^{-1}$ for the latest stage²⁵, i.e. even 10 times faster than those of nitrided α -iron⁵⁵.

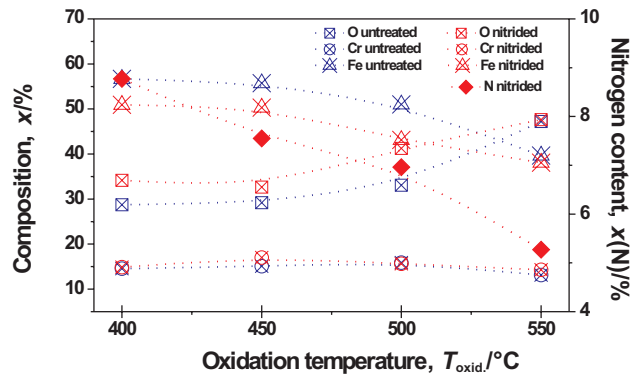


Figure 16: EDS surface composition of the oxidised surfaces of both untreated (blue) and nitrided (red) as a function of the oxidation temperature

Slika 16: EDS-sestava oksidirane površine nenitrirane (modro) in nitrirane površine v odvisnosti od temperature oksidacije

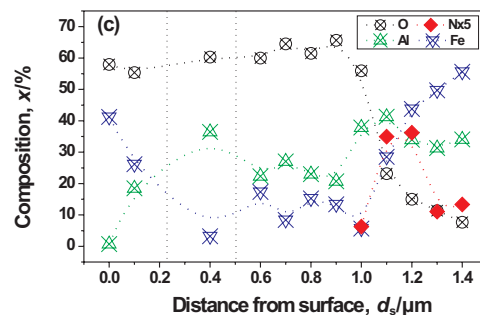
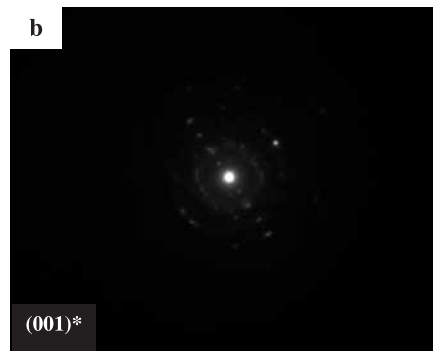
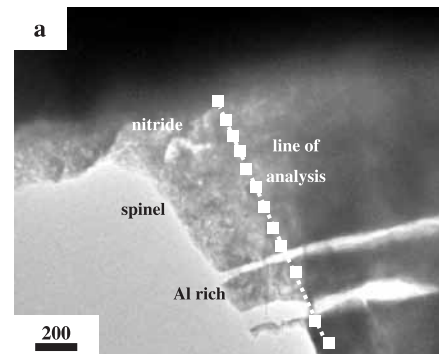


Figure 17: (a) Bright field TEM image of the stratified oxide scale, (b) SADP at the inner scale/substrate interface and (c) EDS microanalyses across all the layers

Slika 17: (a) TEM-slika v svetlem polju za plastasti oksidni sloj, (b) SADP na medploskvi notranja plast škajke/podlaga in (c) EDS-analiza po prerezu vseh plasti

After cooling, the oxide scales are shown to extensively spall off, depicting at least two subscales, a very convoluted top layer and an inner layer with white needles. Although the surface EDS microanalysis and XRD only indicated the presence of iron oxide (hematite), TEM inspection reveals a more complex oxide scale [Figure 17 (a)]. As shown in Figure 17 (b), the selected area diffraction patterns (SADPs) at the top and bottom inner scale suggests the existence of the FeAl_2O_4 phase, with a contribution of hexagonal AlN at the oxide/substrate interface, whose reflections are summarised in Table 5. The EDS (3 nm spot) microanalyses across the entire scale [Figure 17 (c)] confirm that the outermost oxide layer is only composed of iron and oxygen and is about 0.25 μm thick. According to the XRD patterns²⁵ this phase has been identified as $\alpha\text{-Fe}_2\text{O}_3$. Underneath, a 0.2 μm thick layer exists, which is mostly enriched in aluminium, which may correspond to $\alpha\text{-Al}_2\text{O}_3$. The inner oxide layer is the largest (about 0.5 μm thick) with more of Al than Fe, hence suggesting the presence of the FeAl_2O_4 phase found by SADP. At the spinel substrate interface nitrogen is found to concentrate, accompanied with a drop in the oxygen content.

Table 5: Experimental d -spacings obtained from SADPs at the inner oxide layer / substrate interface after oxidation at 800 °C of the nitrided ODS FeAl and their correspondence to the planes of the identified compounds.

Tabela 5: Eksperimentalne d -razdalje iz SADPs na medpovršini notranja oksidna plast/podlaga po oksidaciji nitrirane ODS FeAl pri 800 °C in njihova lega glede na ravnine identificirane spojine

d -spacing, nm	FeAl_2O_4 (JCPDS 34-192)	AlN (JCPDS 25-1133)
0.465	111	–
0.270	–	100
0.246	311	002
0.204	400	–
0.186	331	102
0.139	–	103

Such complex structure allows to shed some light on the oxidation mechanisms after nitridation of ODS FeAl. Although outward diffusion of indium (isoelectronic with aluminium) is two times faster than that of iron in $\text{Fe}_{66}\text{Al}_{34}$ and $\text{Fe}_{50}\text{Al}_{50}$ ⁴⁷, there is not enough aluminium available at the top surface to form the oxide since this is trapped as AlN throughout the compact layer. At the diffusion layer, $\alpha\text{-Fe}$ was found to segregate at the fragmented FeAl matrix together with some AlN. Such iron is readily available for outward diffusion through the important number of short circuit paths that represent the grain boundaries and defects created upon nitridation. However, once the outer iron scale is developed, the oxygen partial pressure decreases and only aluminium oxide is able to form owing to its higher thermodynamic stability. At reduced pressure only the $\alpha\text{-Al}_2\text{O}_3$ phase should develop but its reaction with either Fe_2O_3 ⁵⁶ or FeO ⁵⁷, a FeAl_2O_4 spinel oxide forms. At reduced oxygen partial pressures dissolution of AlN also

takes place⁵⁸ and indeed, no nitrogen is found in any of the oxide layers except at the spinel / substrate interface. This implies that after dissolution of the nitride, nitrogen seems to diffuse further inwardly towards the substrate whereas the resulting aluminium tends to be transported outwardly, stabilising the spinel oxide phase. In previous works⁵⁹ it was already claimed that the spinel layer would only be partially effective in hindering outward aluminium diffusion when the grains coarsened with increasing temperature.

4 SUMMARY AND CONCLUSIONS

Similar low energy, high flux nitridation processing conditions on different fcc metallic substrates lead to very different results depending on the chemical composition of the matrix. It has been shown that pure nickel does not develop an expanded austenite phase due to rejection of nitrogen. The tiny retained amount of nitrogen creates blisters and pores as nitrogen tries to be triggered off the substrate. The major surface roughness is then developed by sputtering. On the contrary, with the addition of chromium an expanded austenite phase develops but nitrogen uptake is still limited by nickel rejection. In turn, iron atoms can thermodynamically favour nitrogen uptake at least at the outermost surface. The higher the nitrogen intake, the higher the degree of deformation including grain swelling, which leads to rougher and harder surfaces. On the contrary, in the presence of Al (ODS FeAl alloy) brings about the formation of an outer AlN compact layer and an inner diffusion layer in which AlN, $\alpha\text{-Fe}$ segregation and fragmentation of the FeAl grains occur. Deformation of the material also seems to be induced upon implantation.

The high temperature oxidation behaviour seems to depend thereafter of the microstructure and chemistry of the implanted specimens. Whereas in pure Ni nitridation does not basically change the oxidation kinetics, on Ni20Cr the kinetics are increased by one order of magnitude. This is mainly due to trapping of chromium by the implanted nitrogen, hence impeding the formation of the protective Cr_2O_3 scale. For the longest exposures enough chromium flux from the matrix seems to be ensured. Deformation induces oxide scale spallation as shown in nitrided Ni. In the AISI 304L stainless steel oxidation of the nitrided specimens brings about progressive disappearance of the γ_{N} phase accompanied with the appearance of an α phase and precipitation of fcc CrN nitride. This phase transformation phenomenon, in turn, may supply chromium to the oxide scale, since the nitrided samples have shown to be enriched in this metal in comparison with the untreated steel. Our results suggest that oxidation seems to proceed by oxygen inward diffusion through the more nitrogen rich planes composing the grains. In the nitrided ODS FeAl aluminium is trapped as AlN, therefore allowing the formation of a non protective outer Fe_2O_3 scale. Once the oxygen partial pressure is reduced dissolution of AlN occurs. Thereafter, nitrogen is further transported

inwardly, whereas aluminium diffuses outwardly. As a result, the FeAl_2O_4 spinel inner layer is developed under the Fe_2O_3 top layer. Therefore, the nitridation treatment changes the oxidation mechanisms. Overall, the role of implanted nitrogen is to retard the establishment of an external alumina scale, but does not seem to impede it. Longer oxidation tests should be carried out to confirm this possibility.

Acknowledgments

J.P. Rivière and G. Abrasonis from the LMP laboratory at Poitiers (France) are gratefully acknowledged for the nitridation experiments. These acknowledgments are also extended to various colleagues of the LEMMA laboratory (G. Bonnet, J. F. Dinhut, J. L. Grosseau-Poussard, J. Balmain and C. Savall) for carrying out some of the experiments and for fruitful discussion.

5 REFERENCES

- ¹ A. M. Jones, S. J. Bull Surf. Coatings Technol. 83 (1996), 269
- ² S. Picard, J. B. Memet, R. Sabot, J. L. Grosseau-Poussard, J. P. Rivière, R. Meilland, Mater. Sci; Eng. A 303 (2001), 163
- ³ Z. L. Zhang, T. Bell, Surf. Eng. 1 (1985), 131
- ⁴ C. Blawert, H. Kalvelage, B. L. Mordike, G. A. Collins, K. T. Short, Y. Jiraskova, O. Schneeweiss, Surf. Coatings Technol. 136 (2001), 181
- ⁵ J. P. Rivière, P. Méheust, J. P. Villain, C. Templier, M. Cahoreau, G. Abrasonis, L. Pranevicius, Surf. Coatings Technol. 158–159 (2002) 99
- ⁶ J. P. Rivière, M. Cahoreau, P. Méheust, J. Appl. Phys. 91 (2002) 10, 6361
- ⁷ C. T. Sims, N. S. Stoloff, W. C. Hagel, Super alloys II, John Wiley & Sons, Inc. Chichester (1987)
- ⁸ P. K. Aw, A.W. Bachelor, N. L. Loh, Surf. Coatings Technol. 89 (1997), 70
- ⁹ P. K. Aw, A. W. Bachelor, N. L. Loh, Wear 208 (1997), 226
- ¹⁰ C. Leroy, T. Czerwiec, C. Gabet, T. Belmonte, H. Michel, Surf. Coatings Technol. 142–144 (2001), 241
- ¹¹ H. He, T. Czerwiec, C. Dong, H. Michel, Surf. Coatings Technol. 163–164 (2003), 331
- ¹² F. Pedraza, J. L. Grosseau-Poussard, G. Abrasonis, J. P. Rivière, J. F. Dinhut, J. Appl. Phys. 94 (2003), 7509
- ¹³ F. Pedraza, C. Savall, G. Abrasonis, J. P. Rivière, J. F. Dinhut, J. L. Grosseau-Poussard, Thin Solid Films 515 (2007), 3661
- ¹⁴ D. Williamson, J. A. Davis, P. J. Wilbur, Surf. Coatings Technol. 103–104 (1998), 178
- ¹⁵ J. P. Rivière, P. Méheust, J. A. García, R. Martínez, R. Sánchez, R. Rodríguez, Surf. Coatings Technol. 158–159 (2002), 295
- ¹⁶ A. Lasalmonie, Intermetallics 14 (2006), 1123
- ¹⁷ S. Thongtem, T. Thongtem, M. J. McNallan, Surf. Interface Anal. 28 (1999) 1, 61
- ¹⁸ J. Magnan, G. C. Weatherly, M. C. Cheynet, Met. Mat. Trans. 30A (1999) 1, 19
- ¹⁹ B. Zhao, J. Sun, J. S. Wu, Z. X. Yuan, Scripta Mater. 46 (2002), 581
- ²⁰ C. L. Chu, S.K. Wu, Surf. Coatings Technol. 78 (1996), 219
- ²¹ T. K. Roy, R. Balasubramaniam, A. Gosh, Met. Mat. Trans. 27A (1996) 12, 3993
- ²² T. K. Roy, R. Balasubramaniam, A. Gosh, Met. Mat. Trans. 27A (1996) 12, 4003
- ²³ H. C. Choe, Surf. Coatings Technol. 148 (2001), 77
- ²⁴ B. Zhao, J. Wu, J. Sun, B. Tu, F. Wang, Intermetallics 9 (2001), 697
- ²⁵ C. Dang Ngoc Chan, C. Huvier, J. F. Dinhut, Surf. Coatings Technol. 165 (2003), 119
- ²⁶ Y. Ando, S. Tobe, H. Tahara, T. Yoshikawa, Vacuum 65 (2002), 403
- ²⁷ Outokompu HSC Chemistry for Windows, Outokompu Research Oy, Pori, 1994
- ²⁸ R. Wei, Surf. & Coatings Technol. 83 (1996), 218
- ²⁹ J. P. Rivière, C. Brin, Ph. Méheust, J. P. Villain, R. Cauvin J. Phys. IV 11 (2001), 71
- ³⁰ E. Menthe, K. T. Rie, Surf. Coatings Technol. 116–119 (1999), 199
- ³¹ M. P. Fewell, D. R. G. Mitchell, J. M. Priest, K. T. Short, G. A. Collins, Surf. Coatings Technol. 131 (2000), 300
- ³² K. Marchev, R. Hidalgo, M. Landis, R. Vallerio, C. V. Cooper, B. C. Giessen, Surf. Coatings Technol. 112 (1999), 67
- ³³ K. Marchev, R. Hidalgo, M. Landis, R. Vallerio, C. V. Cooper, B. C. Giessen, Surf. Coatings Technol. 116–119 (1999), 184
- ³⁴ B. E. Warren, X-Ray Diffraction, Dover, New York (1990)
- ³⁵ H. K. Sanghera, J. L. Sullivan, Surf. Interface Anal. 27 (1999), 678
- ³⁶ G. Abrasonis, J.P. Rivière, C. Templier, A. Déclemy, L. Pranevicius, X. Milhet J. Appl. Phys. 97 (2005) 8, 3531
- ³⁷ L. Pranevicius, C. Templier, J. P. Rivière, P. Méheust, L. L. Pranevicius, G. Abrasonis, Surf. Coatings Technol. 135 (2001), 250
- ³⁸ L. Pranevicius, L. L. Pranevicius, D. Milcius, S. Muzard, C. Templier, J. P. Rivière, Vacuum 72 (2004), 161
- ³⁹ M. F. Denanot, J. Delafond, J. Grilhé, Rad. Effects 88 (1986), 145
- ⁴⁰ A. P. Matthews, M. Iwaki, Y. Horino, M. Satou, K. Yabe, Nucl. Inst. Meth. Phys. Res. B59/60 (1991), 671
- ⁴¹ F. Pedraza, M. Reffass, G. Abrasonis, C. Savall, J. P. Rivière, Surf. Coatings Technol. 176 (2004), 236
- ⁴² B. Clausen, T. Lorentzen, M. A. M. Bourke, M. R. Daymond, Mat. Sci. Eng. A259 (1999), 17
- ⁴³ F. Pedraza, J. L. Grosseau-Poussard, Thin Solid Films 467 (2004), 140
- ⁴⁴ M. Hansen, K. Anderko, Constitution of Binary Alloys 2nd Ed. McGraw-Hill Co. Inc., New York (1958), 984
- ⁴⁵ A. A. Kodentsov, M. J. H. Van Dal, C. Cserhati, L. Daroczi, F. J. J. Van Loo, Acta Mater. 47 (1999), 3169
- ⁴⁶ W. Möller, S. Parascandola, T. Tebizova, R. Günzel, E. Richter, Surf. Coatings Technol. 136 (2001), 73
- ⁴⁷ H. Mehrer, M. Eggersmann, A. Gude, M. Salamon, B. Sepiol, Mat. Sci. Eng. A239-240 (1997), 889
- ⁴⁸ P. Kofstad, High Temperature Corrosion, Elsevier Applied Science Publishers, Ltd. Essex, 1988, 61
- ⁴⁹ F. J. Pérez, M. J. Cristóbal, M. P. Hierro, F. Pedraza, Surf. Coatings Technol. 120–121 (1999), 442
- ⁵⁰ F. Pedraza, PhD Thesis. Universidad Complutense de Madrid, 1998
- ⁵¹ S. Mändl, R. Günzel, E. Richter, W. Möller, B. Rauschenbach, Surf. Coatings Technol. 128–129 (2000), 423
- ⁵² W. Liang, X. Bin, Y. Zhiwei, S. Yaqin, Surf. Coatings Technol. 130 (2000), 304
- ⁵³ M. A. El Khakani, G. Marest, N. Moncoffre, J. Tousset, Nucl. Inst. Meth. Phys. Res. B59/60 (1991), 817
- ⁵⁴ O. Öztürk, D. L. Williamson, Surf. Coatings Technol. 158–159 (2002), 288
- ⁵⁵ R. H. Jutte, B. J. Koi, A.J. Sommers, E-J. Mittemeijer, Oxid. Met. 48 (1997), 87
- ⁵⁶ T. Fujimura, S. I. Tanaka, J. Mater. Sci. 34 (1999), 425
- ⁵⁷ S. E. Sadique, M. A. H. Mollah, M. M. Ali, M. M. Haque, S. Basri, M. M. H. M. Ahmad, S. M. Sapuan, Oxid. Met., 54 (2000) 5–6, 385
- ⁵⁸ C. H. Xu, W. Gao, Y. D. He, Scripta. Mater. 42 (2000), 975
- ⁵⁹ F. Pedraza, J. L. Grosseau-Poussard, J. F. Dinhut, Intermetallics 13 (2005), 27